ACS OMEGA

Open Access

http://pubs.acs.org/journal/acsodf

Article

Numerical Study on Enhanced Heat Transfer of Downhole Slotted-Type Heaters for In Situ Oil Shale Exploitation

Tengfei Sun,[†] Hao Liu,*[,†] Tingjun Yan, and Yang Zhang*

Cite This: *ACS Omega* 2023, 8, 36043−36052

Read Online

ACCESS | Metrics & More | Article Recommendations

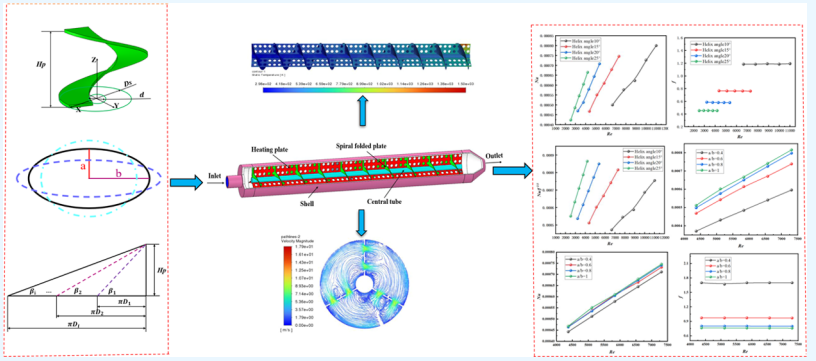

ABSTRACT: In order to improve the flow state of the heater shell side and enhance the performance evaluation of the heater, this paper proposes a perforated plate-type heater model. Based on Fluent, numerical studies are conducted on the heat transfer performance and shell-side fluid flow characteristics of a perforated plate-type heater. The variations of the heat transfer factor *Nu*, friction factor *f*, and evaluation parameter $Nu/f^{1/3}$ are analyzed for different helix angles β and ratios of the long and short semiaxes of the circular holes on the heating plate under different Reynolds numbers *Re*. The results reveal that under the same shell-side Reynolds number *Re*, the heat transfer factor *Nu* shows an increasing trend with the increase in the proportion of the helix angle β. The heat transfer factor *Nu* for the heating plate with the hole shape ratio $a/b = 1$ does not exhibit significant improvement compared to hole shape ratios $a/b = 0.8$ and $a/b = 0.6$, but it increases by 4.87 to 7.07% compared to the hole shape ratio $a/b = 0.4$ in the perforated plate-type heater. On the other hand, the friction factor *f* decreases as the helix angle β and the ratio of hole shapes on the heating plate increase. The lowest friction factor *f* is observed for the helix angle β of 25° and the hole shape ratio $a/b = 1$ in the perforated plate-type heater. When the helix angle β is 25° and the hole shape ratio is $a/b = 1$, the evaluation parameter $Nu/f^{1/3}$ reaches its highest value, indicating the optimal overall performance of the perforated plate-type heater.

1. INTRODUCTION

Oil shale is an abundant unconventional oil and gas resource.[1,2] According to incomplete statistics, it is found in over 30 countries worldwide, with reserves estimated at around 419.6 billion barrels, accounting for approximately 13% of global oil reserves. Effective development of oil shale can reduce dependence on crude oil, utilize resources efficiently, reduce environmental pollution, enhance energy security, and promote economic development.[3] With the continuous development of oil shale extraction technology, in situ heating of oil shale has emerged as a new direction in oil shale development.[4] In situ heating of oil shale involves the conversion of electrical energy into heat energy, which is then used to heat the oil shale formation through conduction or the generation of high-temperature fluids.[5] Compared to traditional retorting techniques, in situ heating of oil shale offers significant advantages. It improves recovery efficiency, reduces operational costs, and minimizes the environmental impact. Currently, there are issues with insufficient heat transfer of gas in the shell of the in situ heating device for shale oil mining wells, resulting in high heating costs and low outlet temperatures. Therefore, in situ heating of shale oil places higher demands on enhancing heat transfer in the downhole heating device.[6−12]

Currently, research on the heat transfer and flow performance of orifice-type heaters with baffles has mainly focused on the form, structure, presence or absence of central tubes, and shell design of the baffles without considering the influence of the orifice proportion of the heating plate on the heat transfer

Received: June 9, 2023
Accepted: August 24, 2023
Published: September 20, 2023

and flow performance. Wang et al.[6] found through experiments that under the same Reynolds number *Re*, the entropy generation number loss of the continuous helical baffle heater was reduced by 30% compared to the bow-shaped baffle heater. Peng et al.[7] conducted numerical simulation studies on the heat transfer and flow performance of the helical baffle heater and found that the continuous helical baffle heater had a heat transfer performance improvement of about 10% compared to the bow-shaped baffle heater. Yang et al.[8] conducted numerical simulation studies on single-helix and double-helix continuous helical baffle heat exchangers and found that the double-helix structure had good heat transfer performance with low pressure drop. Sun[9] conducted numerical simulation studies on the flow performance, heat transfer coefficient, and pressure drop of cross-flow baffle heaters and helical baffle heaters and found that the helical baffle heater reduced dead zones and backflow by helical flow and had a uniform wall temperature distribution on the heating tube, with a smaller shell-side pressure drop. Lutcha and Nemcansky[10] conducted experimental studies on the central tube of the heater and found that under the same Reynolds number *Re*, the heat transfer factor *Nu* of the heater without a central tube was significantly higher than that of the heater with a central tube. Stehlik et al.[11] used the Bell-Delaware method to summarize various variables that affect the heat transfer and flow performance of helical baffle heat exchangers as turbulence enhancement factors and provided dimensionless criterion curves for various factors. Guo et al.[12] found that continuous helical baffle heaters have the advantages of no flow direction abrupt changes, uniform flow, no dead zones, and continuous support for electric heating plates by the helical structure, which is less prone to induce vibrations. The paper proposes an innovative structure for an orifice-type heater, namely, the underground continuous spiral baffle orifice-type heater. In comparison to the spiral heater mentioned earlier,[6−12] this orifice-type heater incorporates a spiral baffle and plate orifice heating plate structure within the shell side. The gas inside the shell side flows in a double "O"-type spiral, with a smooth and uniform flow direction, without any sudden changes or dead zones. Additionally, the design increases the path and heating time of the fluid within the shell-side heater, thereby improving the heating efficiency of the heater. This improvement is beneficial for the extraction and production of shale oil.

This review presents a perforated plate-type heater structure and conducts numerical simulations on the flow and heat transfer performance of the heater with different helix angles β and different ratios of hole types on the heating plate. The design of the helical baffle plate structure is also analyzed, and the helical angle β of the helical baffle plate is defined. Through numerical simulations, the heat transfer factor *Nu*, friction factor *f*, and evaluation index $Nu/f^{1/3}$ of the perforated plate-type heater are studied under different heating plate hole type ratios and helix angles β, as they vary with different Reynolds numbers *Re*. By comparing and analyzing the results, a perforated plate-type heater model with better performance is determined. The numerical analysis results provide a theoretical basis for the subsequent manufacturing of the perforated plate-type heater structure and better serve the field of oil shale exploitation.

2. MODEL AND CONTROL EQUATIONS

2.1. Physical Model. A simplified geometric model of the orifice-plate-type heater was established by using SolidWorks software. The structure of the orifice-plate-type heater is relatively complex during the heating process. This paper mainly focuses on the numerical study of enhanced heat transfer in an orifice-plate-type heater. To reduce the computational difficulty of numerical simulation, the model was simplified to include only the shell, central tube, orifice-plate-type heating plate, and continuous helix baffle. The thermal stress and deformation caused by heating during the operation of the heater were ignored, as were the gaps between the central tube, heater shell, orifice-plate-type heating plate, and continuous helix baffle.[13−15]

The perforated plate-type heater mainly consists of a shell, a central tube, a perforated plate-type heating plate, and a continuous helix flow deflector, with dimensions shown in Table 1 and the physical model shown in Figure 1. In this study, the adjacent perforated plate-type heating plates in the heater are connected seamlessly with an angle of 120°; one end is connected seamlessly with the shell, and the other end is connected seamlessly with the central tube. The gas flows in an "O"-shaped helix in the heater, which reduces the pressure drop of the fluid in the shell and makes the heat transfer more uniform, reducing the occurrence of local high temperature in the perforated plate-type heating plate and improving the life of the heater. The diameter of the circular hole on the perforated heating plate is 16 mm. The distance between the upper side of the hole and the upper side of the heating plate is 15 mm. The center-to-center distance between the upper and lower holes is 30 mm, and the center-to-center distance between adjacent holes is 26 mm. The inner diameter and length of the shell are 150 and 1300 mm, respectively. The diameter and length of the central tube are 30 and 1200 mm, respectively. The inner diameters of the inlet and outlet ports are both 50 mm. The continuous helix flow deflector has a length of 1200 mm and a thickness of 2 mm. The helix angles

Table 1. Physical Model Size Parameters of the Orifice-Plate-Type Heater

parameter name	size description	parameter name	size description
outer diameter of shell/mm	160	width of orifice-plate-type heating plate/mm	60
inner diameter of shell	150	thickness of orifice-plate-type heating plate/mm	2
length of helical baffle plate/mm	1200	length of orifice-plate-type heating plate/mm	1200
thickness of helical baffle plate/mm	2	diameter of circular holes in orifice-plate-type heating plate/mm	16
diameter of center tube	30	outlet inner diameter/mm	50
inlet inner diameter/mm	50	outlet outer diameter/mm	60
inlet inner diameter/mm	60		
helix angle/°		10, 15, 20, 25	
number of orifice-plate-type heating plates/pc		3	
layout mode of orifice-plate-type heating plate		Uniformly arranged at 120° in circumference.	

https://doi.org/10.1021/acsomega.3c04099
ACS Omega 2023, 8, 36043−36052

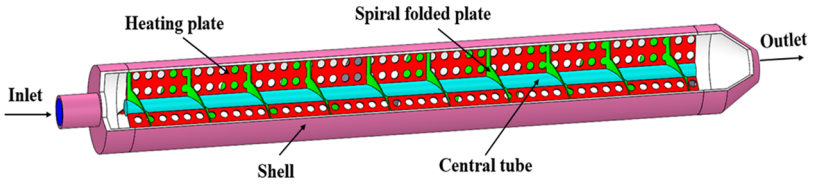

Figure 1. Physical model calculation domain diagram of the orifice-plate-type heater.

used in this study are 10, 15, 20, and 25°, with corresponding labels of β10, β15, β20, and β25°, respectively.

Within the scope of this study, an analysis of the hole shape of the orifice-plate-type heating plate was conducted. The method of setting the perimeter of the ellipse equal to the circumference of a circle was used to approximate the width "a" and length "b" of the ellipse using eq 1.[16] As shown in Figure 2, the effects of four types of hole shapes with diameter

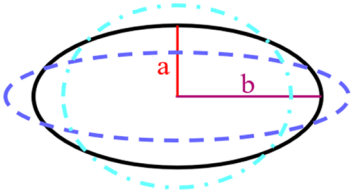

Figure 2. Variation diagram of the hole shape.

ratios of 0.4, 0.6, 0.8, and 1 and a helix angle of 15° on the enhanced heat transfer of the heater were studied, and numerical simulations were conducted for each of the four hole shapes.

$$p = 2\pi\sqrt{\frac{1}{2}(a^2 + b^2)} \tag{1}$$

where p represents the perimeter of the ellipse, mm; a represents the semiminor axis, mm; and b represents the semimajor axis, mm.

2.2. Design and Analysis of Helical Baffles. The helix angle β is an important parameter in the design process of the heater, and in this article, it is defined as the angle between the tangent line of the outermost helical curve of the helical baffle and the horizontal plane.[17] As shown in Figure 3, it is a

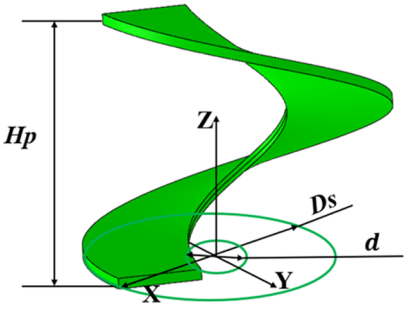

Figure 3. Schematic diagram of the helical baffle within one cycle.

schematic diagram of the helical baffle within one helical cycle, where H_p is the pitch of the helical baffle, d is the diameter of the central tube, and D_s is the outer diameter of the helical baffle.

The straightened outermost helical curve of the helical baffle can be used to obtain the schematic diagram for calculating the helix angle β of the helical baffle, as shown in Figure 4, where β_i represents the helix angle β of the helical baffle at the corresponding location d_i.

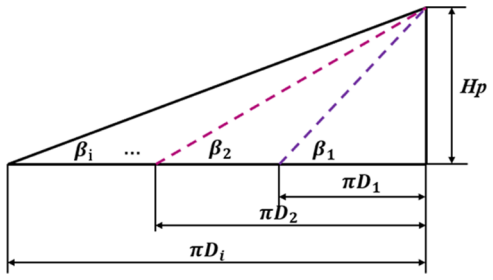

Figure 4. Helix baffle helix angle β calculation schematic diagram.

As shown in Figure 4, it can be known by analyzing the geometric relationship that

$$H_p = \pi D_1 \tan\beta_1 = \pi D_2 \tan\beta_2 = \cdots = \pi D_i \tan\beta_i = \pi D_s \tan\beta \tag{2}$$

According to eq 2, it can be seen that helix angle β is proportional to the pitch and inversely proportional to the outer diameter of the helical baffle. When the outer diameter of the helical baffle remains unchanged, the pitch of the heater can be changed by changing the magnitude of the helix angle β.

2.3. Control Equation. During the flow and heating process of air in an orifice-plate-type heater, the mass conservation equation, momentum conservation equation, and energy conservation equation are followed. The control equations in the calculation process are expressed as follows[18−20]

The conservation of mass equation is

$$\frac{\partial\rho}{\partial t} + \frac{\partial(\rho u_x)}{\partial x} + \frac{\partial(\rho u_y)}{\partial y} + \frac{\partial(\rho u_z)}{\partial z} = 0 \tag{3}$$

where ρ is the fluid density, kg/m^3; t is the time, s; and the x, y, and z components of velocity u are represented by u_x, u_y, and u_z, m/s, respectively.

The conservation equation of momentum in the x-direction is

$$\frac{\partial(\rho u_x)}{\partial t} + \nabla\cdot(\rho u_x \boldsymbol{u}) = \frac{\partial p}{\partial y} + \frac{\partial(\tau_{xx})}{\partial x} + \frac{\partial(\tau_{yx})}{\partial y} + \frac{\partial(\tau_{zx})}{\partial z} + F_x \tag{4}$$

The conservation equation of momentum in the y-direction is

https://doi.org/10.1021/acsomega.3c04099
ACS Omega 2023, 8, 36043−36052

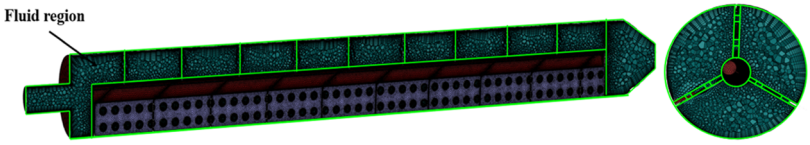

Figure 5. Fluid grid of the orifice plate heater.

Table 2. Grid Number and Number Correspond to the Table

numbering	1	2	3	4	5
number of grids	1,804,369	2,275,638	2,682,436	3,272,635	3,769,254

$$\frac{\partial(\rho u_y)}{\partial t} + \nabla\cdot(\rho u_y \boldsymbol{u}) = \frac{\partial p}{\partial y} + \frac{\partial(\tau_{xy})}{\partial x} + \frac{\partial(\tau_{yy})}{\partial y} + \frac{\partial(\tau_{yz})}{\partial z} + F_y \quad (5)$$

The conservation equation of momentum in the z-direction is

$$\frac{\partial(\rho u_z)}{\partial t} + \nabla\cdot(\rho u_z \boldsymbol{u}) = \frac{\partial p}{\partial y} + \frac{\partial(\tau_{xz})}{\partial x} + \frac{\partial(\tau_{yz})}{\partial y} + \frac{\partial(\tau_{zz})}{\partial z} + F_z \quad (6)$$

where p is the pressure acting on a fluid element, Pa; the viscous force on x, y, and z are represented by τ_x, τ_y, and τ_z, Pa, respectively; F_x, F_y, and F_z are the components of the external force F acting on the element in the x, y, and z directions, N, respectively; and $\boldsymbol{u}$ is the velocity vector, m/s.

The conservation equation of energy is

$$\frac{\partial(\rho T)}{\partial t} + \mathrm{div}(\rho T \boldsymbol{u}) = \mathrm{div}\left(\frac{k}{C_p}\mathrm{grad}\ T\right) + S_T \quad (7)$$

where C_p is the specific heat capacity at constant pressure, KJ/(kg·K); T is the temperature of the fluid element, K; k is the thermal conductivity coefficient of the air element, W/(m·K); and S_T is the viscous dissipation term of the fluid element.

In the heating process of a continuous helix baffle heat exchanger, there is strong swirling and secondary flow in the shell-side channel, and the flow exhibits high anisotropy.[21,22] The RNG $k-\varepsilon$ model performs better than the standard $k-\varepsilon$ model in the calculation of strong streamline bending and rotation. Currently, most numerical simulation studies of helix baffle heat exchangers also use the RNG $k-\varepsilon$ model.[23−26] In order to better study the numerical simulation process of airflow and heating in the shell side of the helix baffle heat exchanger, the RNG $k-\varepsilon$ turbulence model is adopted in this study.

The turbulent kinetic energy k equation is

$$\frac{\partial(\rho k)}{\partial t} + \frac{\partial(\rho k V_i)}{\partial x_i} = \frac{\partial}{\partial x_j}\left(\alpha_k \mu_{\mathrm{eff}}\frac{\partial k}{\partial x_j}\right) + G_k + \rho\varepsilon \quad (8)$$

The turbulent dissipation rate ε equation is

$$\frac{\partial(\rho \varepsilon)}{\partial t} + \frac{\partial(\rho \varepsilon V_i)}{\partial x_i} = \frac{\partial}{\partial x_j}\left(\alpha_k \mu_{\mathrm{eff}}\frac{\partial \varepsilon}{\partial x_j}\right) + C_{1\varepsilon}^{*}\frac{\varepsilon}{k}G_k + C_{2\varepsilon}\rho\frac{\varepsilon^2}{k} \quad (9)$$

where

$$\mu_{\mathrm{eff}} = \mu + \mu_t;\ \mu_t = \rho c_\mu \frac{k^2}{\varepsilon};\ G_k = u_t \frac{\partial V_i}{\partial x_j}\left(\frac{\partial V_i}{\partial x_j} + \frac{\partial V_j}{\partial x_i}\right);\ C_{1\varepsilon}^{*} = C_{1\varepsilon} - \frac{\eta(1-\eta/\eta_0)}{1+\beta\eta^3}$$

$$E_{ij} = \frac{1}{2}\left(\frac{\partial V_i}{\partial x_j} + \frac{\partial V_j}{\partial x_i}\right);\ \eta = (2E_{ij}\cdot E_{ij})^{1/2}\frac{k}{\varepsilon};\ C_\mu = 0.0845;\ C_{1\varepsilon}^{*} = 1.42;\ C_{2\varepsilon} = 1.68;\ \beta = 0.012;\ \eta_0 = 4.38;\ \alpha_k = \alpha_\varepsilon = 1.39$$

3. GRID PARTITIONING AND COMPUTATIONAL METHODS

3.1. Grid Partitioning and Independence Verification.

In the numerical simulation of the grid heater, considering the complexity of the internal structure and fluid flow of the orifice plate heater, an unstructured grid partitioning method is used for the fluid domain. Considering the heat transfer characteristics of the orifice plate heater and the boundary effects of the gas helix flow on the shell side, the orifice plate, center tube, and helix baffle are locally refined. Meanwhile, due to the drastic temperature changes near the wall, an enhanced wall function is used near the wall, as shown in Figure 5, which shows the fluid grid of the orifice plate heater.

A set of 5 grids were chosen to verify the independence of a hole-type heat exchanger with a helix angle β15° and a ratio $a/b = 1$. The number and identification of the grids are shown in Table 2. As shown in Figure 6, when the shell-side Reynolds

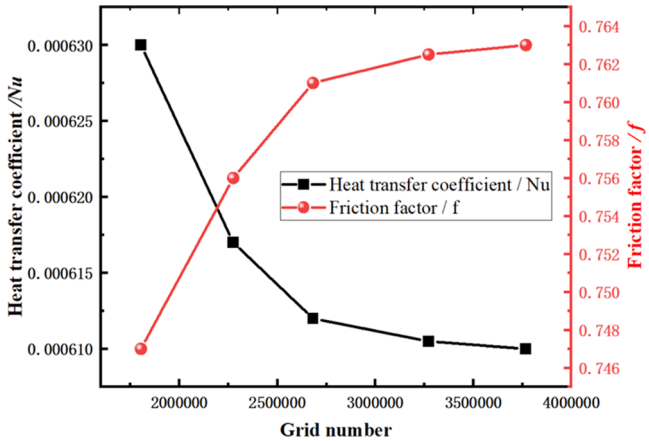

Figure 6. Graph of the variation of heat transfer factor Nu and friction factor f with the grid number.

https://doi.org/10.1021/acsomega.3c04099
ACS Omega 2023, 8, 36043−36052

Table 3. Gas Physical Parameters

physical parameters	density [kg × m^{-3}]	thermal conductivity coefficient [W × (m × K)$^{-1}$]	specific heat capacity [J × (kg × K)$^{-1}$]	dynamic viscosity [kg × (m × s)$^{-1}$]
air	1.225	0.024	1006.43	1.7894 × 10^{-5}

number Re = 5838, the heat transfer coefficient Nu and friction factor f of the hole-type heat exchanger were calculated for the 5 sets of grids. From the figure, it can be seen that as the number of grids increases, the curvature of the heat transfer coefficient Nu and friction factor f decreases, and when the number of grids increases to 2.7 million, the trend of the heat transfer coefficient Nu and friction factor f becomes nearly flat. When the number of grids is greater than that of grid 3, the numerical results are quite close, with the error of the heat transfer coefficient Nu and friction factor f being within 1%.[27,28] Thus, the independence of the grid and the accuracy of the numerical simulation method have been satisfied. Considering the issues of calculation accuracy and computational efficiency, a grid of 2.68 × 10^6 was used for the numerical simulation, and the same grid density was used for other hole-type heat exchangers.

3.2. Calculation Method and Boundary Conditions. When investigating the flow and heat transfer characteristics of the perforated plate-type heater, a perforated heating plate with impermeable and no-slip constant-heat flux wall boundary conditions is employed.[29] The gas physical parameters are listed in Table 3. The heater with different helix angles and hole ratios is subjected to a heating power of 4 kW and five different mass flow rates (0.00974, 0.01137, 0.01299, 0.01462, 0.01624 kg/s). The boundary conditions include mass flow rate inlet with an inlet temperature of 298.15 K and pressure outlet with an outlet pressure of 0 Pa gauge. The turbulence model adopted is the RNG k-epsilon model. During the numerical simulation, the gradient terms are calculated using the least-squares cell-based method. The momentum and energy equations are solved using a first-order upwind scheme, while the turbulent kinetic energy and turbulent dissipation rate are solved using a second-order upwind scheme. The pressure−velocity coupling is handled using the SIMPLE algorithm, and the near-wall treatment is implemented using an enhanced wall function approach. The default values are used for the under-relaxation factors.[30−32] In the iteration process, the residuals of continuity, x-velocity, y-velocity, z-velocity, k, and epsilon are controlled at a level, while the energy equation is controlled at a level. The iteration calculation is considered converged when the residuals reach the corresponding residual accuracy.[33]

The numerical calculations for the perforated plate-type heater are conducted under the following assumptions

(1) The turbulent flow of air in the heater shell side is fully developed and in a steady state.
(2) The gap between the helical baffle plate and the inner wall of the heater shell is neglected.
(3) The gap between the meshed heating plate and the helical baffle plate is neglected.
(4) The gap between the helical baffle plate and the outer wall of the central pipe is neglected.

3.3. Data Processing Method. In order to investigate the heat transfer characteristics of the orifice-type heater, the data obtained from numerical simulation was processed. The relationship between the heat transfer coefficient Nu, the friction factor f, and the shell-side Reynolds number Re of the orifice-type heater was studied.

The definition of the shell-side Reynolds number Re for the orifice-type heater is

$$Re = \frac{U_s \rho_a D_{in}}{u_a} \tag{10}$$

where U_s is the characteristic flow velocity on the shell side, m/s; ρ_a is the air density, kg/m^3; u_a is the dynamic viscosity, kg/m·s; and D_{in} is the characteristic length on the shell side, m.

The definition of the characteristic flow velocity U_s on the shell side for the orifice-type heater is

$$U_s = \frac{M_a}{\rho_a A_{min}} \tag{11}$$

where M_a is the mass flow rate of air, kg/s, and A_{min} is the minimum flow area for air on the shell side, m^2.

The definition of the shell-side heat transfer coefficient h is[34,35]

$$h = \frac{P}{A\Delta t_m} \tag{12}$$

where P is the heating power of the orifice-type heater, W, and A is the heating area of the orifice-type heater plate, m^2.

The definition of heat transfer temperature difference Δt_m is[9]

$$\Delta T_{max} = T_{av} - T_{in} \tag{13}$$

$$\Delta T_{min} = T_{out} - T_{in} \tag{14}$$

When $\frac{\Delta T_{max}}{\Delta T_{min}} \geq 1.7$, Δt_m is calculated using logarithmic mean temperature difference

$$\Delta t_m = \frac{\Delta T_{max} - \Delta T_{min}}{\ln \frac{\Delta T_{max}}{\Delta T_{min}}} \tag{15}$$

When $\frac{\Delta T_{max}}{\Delta T_{min}} < 1.7$, Δt_m is calculated using the arithmetic mean temperature difference

$$\Delta t_m = \frac{\Delta T_{max} + \Delta T_{min}}{2} \tag{16}$$

where T_{av} is the average temperature of the perforated heating plate, K; T_{in} is the temperature at the inlet of the orifice-type heater, K; and T_{out} is the outlet temperature of the orifice-plate-type heater, K.

The definition of the dimensionless heat transfer coefficient Nu for the shell side is[36]

$$Nu = \frac{hD_{in}}{\lambda} \tag{17}$$

where λ is the thermal conductivity coefficient of air, W/(m·K).

The definition of the dimensionless resistance factor f for the shell side is[37]

https://doi.org/10.1021/acsomega.3c04099
ACS Omega 2023, 8, 36043−36052

$$f = \frac{\Delta P D_{in}}{\frac{1}{2}\rho_a U_s} \quad (18)$$

where ΔP is the pressure drop in the shell side of the orifice-type heat exchanger, P_a.

4. HEATER HEAT TRANSFER AND FLOW ANALYSIS

When 0.01624 kg/s of gas is fed into the orifice-type heater, flow and heat transfer performance analysis is carried out on a orifice-type heater with a helix angle β15° and a ratio a/b = 1, using the trace diagram and the distribution cloud diagram of the heating plate wall temperature.

4.1. Analysis of Fluid Flow Performance of the Heater Shell. As shown in Figure 7, a trace cloud diagram of the orifice-type heater is presented. During the heating process, air flows in a double "O"-shaped spiral pattern with uniform velocity, without any dead zones in the flow, which allows for better heat exchange between the orifice-type heating plate and the air while reducing the shell-side resistance. There are some small vortices in the airflow after the air passes through the heating plate in the shell side, causing pressure drop in the heater. The vortex gas on the lee side of the heating plate is fully flushed, promoting sufficient heat exchange of the orifice-type heating plate and avoiding local high temperatures caused by insufficient heat transfer on the lee side of the plate, thus improving the service life of the orifice-type heater.

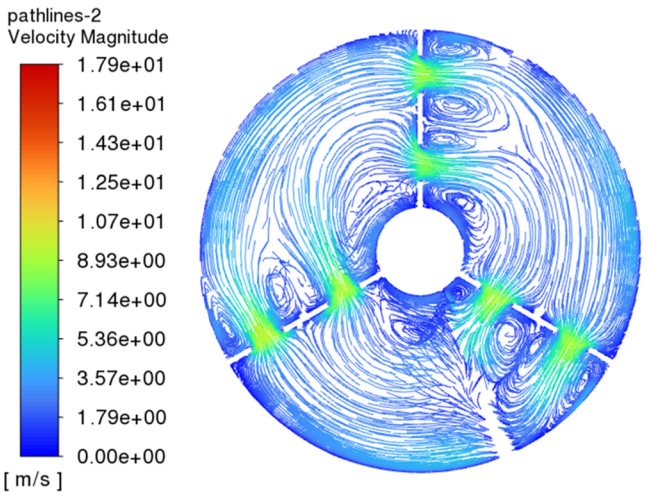

Figure 7. Tracer cloud map of the orifice-type heater.

4.2. Performance Analysis of Heat Transfer of the Orifice-Plate-Type Heating Plate. As shown in Figure 8, a temperature distribution cloud map of the heating plate of the orifice-type heater is presented. During the heating process, air flows in a regular spiral pattern along the spiral deflector plate, uniformly flushing the heating plate wall through the small holes on the orifice-type heating plate. This promotes the uniform heat exchange between the orifice-type heating plate and the air, resulting in a uniform temperature distribution on the orifice-type heating plate wall. The lowest temperature is found at the inlet of the orifice-type heating plate on the left, mainly because when low-temperature gas enters the orifice-type heater, there is a large temperature difference between the orifice-type heating plate and the low-temperature air, which leads to rapid heat transfer between them. As a result, the air takes away some of the heat from the orifice-type heating plate, leading to a rapid increase in air temperature. This area of the orifice-type heater has the highest heat transfer coefficient and thus the lowest temperature on the orifice-type heating plate wall. As air flows in a spiral pattern from the inlet on the left to the outlet on the right, it is continuously and uniformly heated by the orifice-type heating plate, and its temperature gradually increases. The temperature difference between the air and the orifice-type heating plate gradually decreases, leading to a gradual decrease in heat transfer performance, which prevents the temperature on the orifice-type heating plate from increasing gradually from left to right. Although the heat transfer on the orifice-type heating plate is very uniform, there is local high temperature at the outlet on the right. This is mainly because the air in the shell area at the rear of the heater flows out of the outlet without passing through the heating plate in this area. The solution is to remove the area at the rear of the orifice-type heating plate that the air does not pass through, thus avoiding the phenomenon of local high temperature at the end of the orifice-type heating plate and improving the service life of the heater.

5. RESULTS AND DISCUSSION

The magnitudes of the heat transfer factor Nu and resistance factor f are important indicators for evaluating the overall performance of a heater. The evaluation index of $Nu/f^{1/3}$ reflects the synergy of the heater. Therefore, it is of great significance to evaluate the heater based on the index of $Nu/f^{1/3}$.

5.1. Impact of Different Helix Angles on Heat Transfer Performance of the Heater. Based on the design conditions of orifice-type heaters and by controlling other variables, numerical simulations were performed to investigate the effects of different helix angles on the heat transfer factor Nu, the resistance factor f, and the evaluation index $Nu/f^{1/3}$ with respect to the shell-side Reynolds number.

As shown in Figure 9, variation of the heat transfer factor Nu with respect to the shell-side Reynolds number Re is presented. From the graph, it can be observed that the heat transfer factor

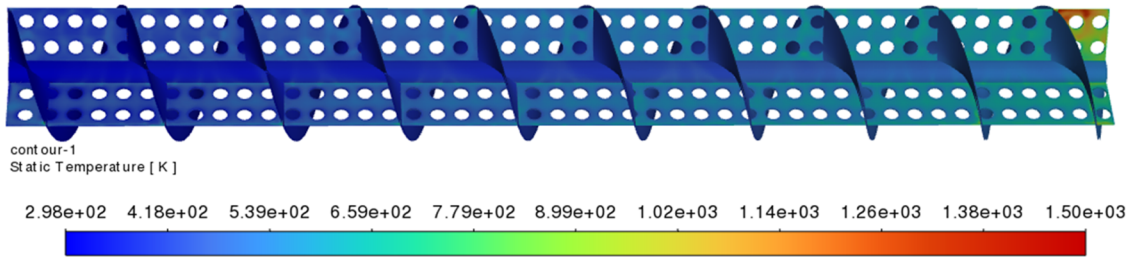

Figure 8. Temperature distribution map of the heated plate wall of an orifice-type heater.

https://doi.org/10.1021/acsomega.3c04099
ACS Omega 2023, 8, 36043−36052

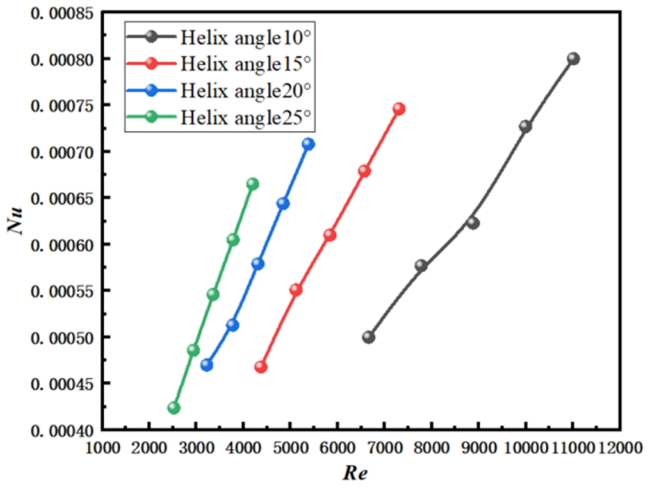

Figure 9. Variation graph of the heat transfer factor *Nu* with respect to the shell-side Reynolds number *Re*.

Nu increases with the increase of the Reynolds number *Re*, and it also varies significantly with the helix angle. Within the range of numerical simulations, at the same shell-side Reynolds number *Re*, the relationship between the heat transfer factor *Nu* and the helix angle is $\beta 25 \geq \beta 20 \geq \beta 15 \geq \beta 10°$.

As shown in Figure 10, the variation graph of the resistance factor *f* with respect to shell-side Reynolds number *Re* is

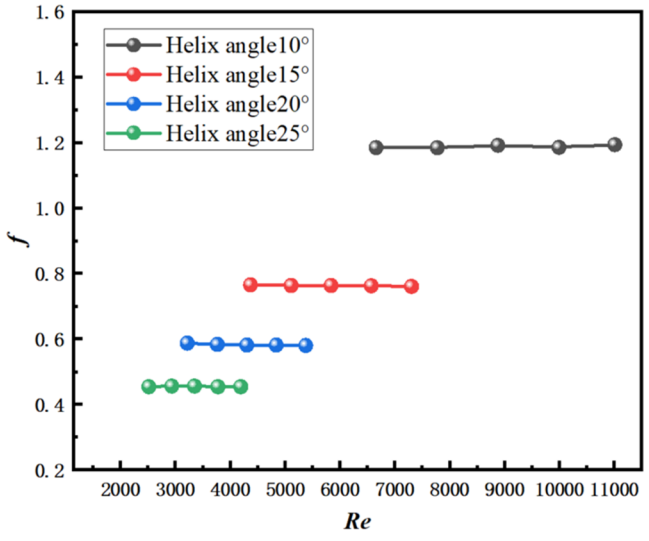

Figure 10. Graph of the variation of the coefficient of friction *f* with the Reynolds number *Re* in a pipe.

presented. From the graph, it can be observed that the resistance factor *f* has almost no significant variation with respect to the shell-side Reynolds number *Re*, but it varies significantly with different helix angles. Within the range of numerical simulations, at the same shell-side Reynolds number *Re*, the relationship between the resistance factor *f* and the helix angle is $\beta 10 \geq \beta 15 \geq \beta 20 \geq \beta 25°$. The resistance factor *f* of the helix angle $\beta 25°$ is reduced by 1.6, 0.68, and 0.28 times compared to the resistance factors *f* of the helix angles $\beta 20$, $\beta 15$, and $\beta 10°$, respectively. Increasing the helix angle β appropriately can reduce the resistance factor *f* of the plate-type heater and thereby reduce the pumping power consumption of the air supplied to the plate-type heater, thus improving the overall efficiency.

As shown in Figure 11, variation of the evaluation index $Nu/f^{1/3}$ with the Reynolds number *Re* is presented. It can be

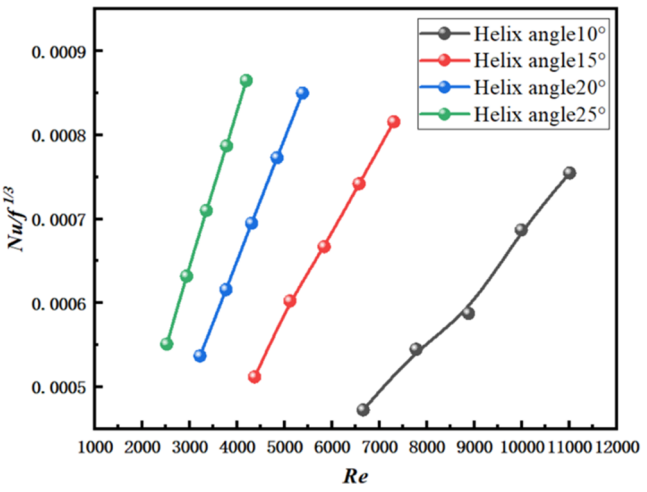

Figure 11. Graph of the variation of the evaluation index $Nu/f^{1/3}$ with the Reynolds number *Re* in a pipe.

observed from the graph that the evaluation index $Nu/f^{1/3}$ increases with the increase of the Reynolds number *Re*, and it also shows a significant variation with the helix angle. Within the range of numerical simulation, under the same Reynolds number *Re*, the relationship between the evaluation index $Nu/f^{1/3}$ and the helix angle is found to be $\beta 25 \geq \beta 20 \geq \beta 15 \geq \beta 10°$. By comparing the helix angles $\beta 25$, $\beta 20$, $\beta 15$, and $\beta 10°$, it is found that the heating performance of the helical baffle plate heat exchanger is highest when the helix angle is $\beta 25°$. Therefore, increasing the helix angle β appropriately can improve the comprehensive performance of the heat exchanger.

The variation of different helix angles not only results in different heat transfer and resistance performance of the heat exchanger but also leads to different irreversible losses of the shell-side air during the heating process. Under the same heating conditions, the smaller the helix angle, the smaller the irreversible loss. Since the range of the Reynolds number *Re* for helix angles $\beta 20$ and $\beta 25°$ is similar and their growth trends are similar as well, in the range of numerical simulation, when the Reynolds number *Re* is relatively small, it is more suitable to use the helix angles $\beta 20°$ and β 25° for the helical baffle plate heat exchanger. When the Reynolds number *Re* is moderate, it is more suitable to use the helix angle $\beta 15°$, and when the Reynolds number *Re* is relatively large, it is more suitable to use the helix angle $\beta 10°$ for the helical baffle plate heat exchanger.

5.2. Impact of Different Perforation Patterns on the Heat Transfer of the Heater. Based on the design conditions of the orifice-plate-type heater, while keeping other variables constant, we numerically simulate the variation of the heat transfer factor *Nu*, resistance factor *f*, and evaluation index $Nu/f^{1/3}$ with the shell-side Reynolds number for different perforation patterns of the orifice-plate-type heater.

As shown in Figure 12, the variation of the heat transfer factor *Nu* with the shell-side Reynolds number *Re* is shown. From the figure, it can be seen that the heat transfer factor *Nu* increases with the increase of Reynolds number *Re*, and the

https://doi.org/10.1021/acsomega.3c04099
ACS Omega 2023, 8, 36043−36052

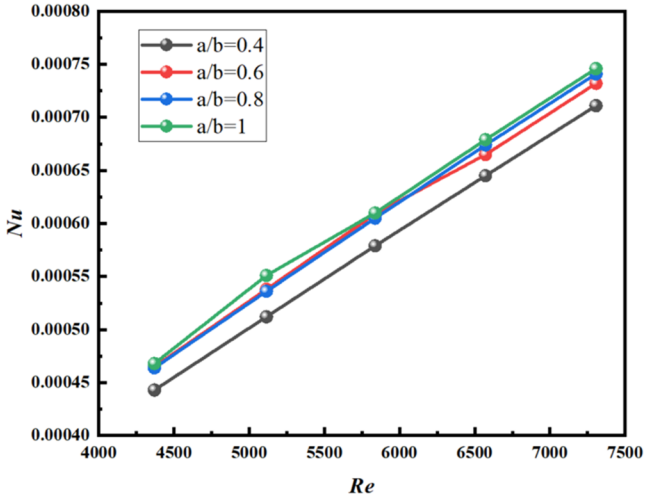

Figure 12. Plot of the variation of the heat transfer factor *Nu* with the shell-side Reynolds number *Re*.

heat transfer factor *Nu* varies with the change of the perforation pattern. The heat transfer factor *Nu* of the orifice-plate-type heater with the perforation ratio $a/b = 1$ is not significantly improved compared with that of the perforation ratios $a/b = 0.8$ and $a/b = 0.6$, but it increases by 4.87−7.07% compared with that of the perforation ratio $a/b = 0.4$.

As shown in Figure 13, the plot of the resistance factor *f* with shell-side Reynolds number *Re* is presented. From the figure, it

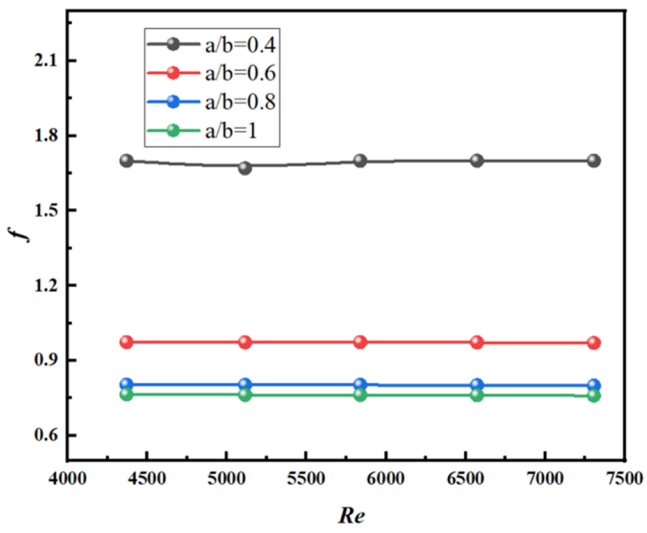

Figure 13. Plot of the variation of the friction factor *f* with the shell-side Reynolds number *Re*.

can be seen that the resistance factor *f* almost remains constant with the shell-side Reynolds number *Re*, but it varies significantly with different perforation patterns. Within the range of numerical simulation, the relationship between the resistance factor *f* and different perforation patterns is $a/b = 1 \geq a/b = 0.8 \geq a/b = 0.6 \geq a/b = 0.4$ at the same shell-side Reynolds number *Re*. The resistance factor *f* of the orifice-plate-type heater with the perforation ratio $a/b = 1$ is 1.2 times, 0.22 times, and 0.09 times lower than that of the perforation ratios $a/b = 0.8$, $a/b = 0.6$, and $a/b = 0.4$, respectively. By comparing the perforation ratios $a/b = 1$, $a/b = 0.8$, $a/b = 0.6$, and $a/b = 0.4$, it is found that the heater has the lowest resistance factor *f* when the perforation ratio is $a/b = 1$. Therefore, the resistance performance of the heater can be reduced by appropriately increasing the perforation ratio of the heating plate.

The plot of the variation of the evaluation index $Nu/f^{1/3}$ with the shell-side Reynolds number *Re* is shown in Figure 14. It

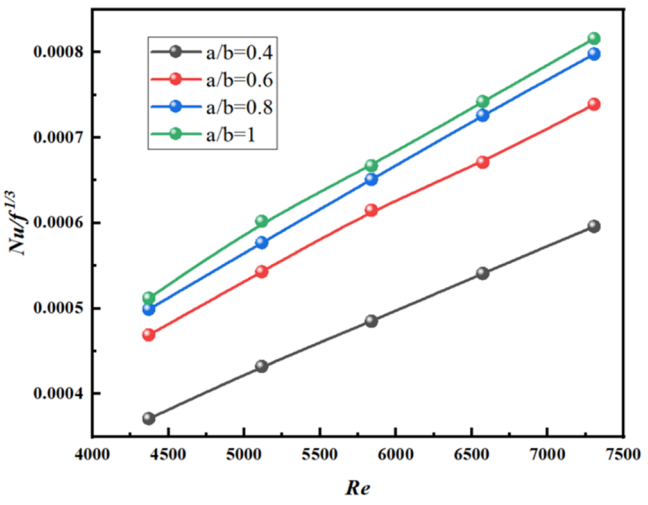

Figure 14. Plot of evaluation metrics $Nu/f^{1/3}$ as a function of the shell-side Reynolds number *Re*.

can be seen from the plot that the evaluation index $Nu/f^{1/3}$ increases with the increase of Reynolds number *Re*, and it also varies significantly with the ratio of the heating plate hole type. Within the range of numerical simulation, the relationship between the evaluation index $Nu/f^{1/3}$ and the hole type ratio is $a/b = 1 \geq a/b = 0.8 \geq a/b = 0.6 \geq a/b = 0.4$, under the same shell-side Reynolds number *Re*. The evaluation index $Nu/f^{1/3}$ of the heating plate with the hole type ratio $a/b = 1$ is higher than that of the heating plate with hole type ratios $a/b = 0.8$, $a/b = 0.6$, and $a/b = 0.4$, with an increase of 2.3−4.3%, 9.2−11.6%, and 36.9−39.4%, respectively. By comparing the hole type ratios $a/b = 1$, $a/b = 0.8$, $a/b = 0.6$, and $a/b = 0.4$, it can be concluded that the heating plate with the hole type ratio $a/b = 1$ has the highest evaluation index $Nu/f^{1/3}$, and the comprehensive performance of the heating plate can be improved by appropriately adjusting the hole type ratio of the heating plate.

6. CONCLUSIONS

Through numerical simulations and comparative analysis of four different helix angles β and four different hole patterns in the plate-type heater without heating, the following conclusions were drawn

(1) Analysis showed that the air in the shell-side outlet of the heater flows directly out of the outlet without passing through the plate-type heater, causing local high temperature on the right side of the outlet. To solve this problem, it is recommended to remove the plate-type heater area where air does not pass through at the tail end, in order to avoid local high temperature at the tail end of the plate-type heater and improve its service life.

(2) According to numerical simulation analysis, the shell-side gas in the orifice-type heater exhibits a double "O"-type spiral flow, with uniform velocity. During the flow

https://doi.org/10.1021/acsomega.3c04099
ACS Omega 2023, 8, 36043−36052

process, there are no dead zones, which is advantageous for the orifice-type heating plate to achieve efficient heat exchange. It prevents the occurrence of localized high temperatures on the leeward side of the heating plate, thus improving the lifespan of the heater. This finding provides potential applications for in situ extraction of oil shale in underground wells.

(3) Under different helix angles β, the heat transfer coefficient *Nu* increases with the Reynolds number *Re*, and *Nu* also shows a significant change with the helix angle. Within the range of numerical simulations, for the same shell-side Reynolds number *Re*, the relationship between the heat transfer coefficient Nu and the helix angle is $\beta 25 \geq \beta 20 \geq \beta 15 \geq \beta 10°$.

(4) Under different hole-pattern ratios on the heating plate, the heat transfer factor *Nu* shows an increasing trend with the shell-side Reynolds number *Re*, and *Nu* also changes with the hole-pattern ratio. There is no significant improvement in *Nu* between the hole-pattern ratios $a/b = 1$, $a/b = 0.8$, and $a/b = 0.6$, but compared with the hole-pattern ratio $a/b = 0.4$, the heat transfer factor *Nu* of the perforated plate-type heater increases by 4.87−7.07%.

(5) When the helix angle of the perforated plate heat exchanger is $\beta 15°$, the performance evaluation index $Nu/f^{1/3}$ of the perforated plate heat exchanger with $a/b = 1$ is improved by 2.3−4.3%, 9.2−11.6%, and 36.9−39.4% compared to the perforated plate heat exchanger with $a/b = 0.8$, $a/b = 0.6$, and $a/b = 0.4$, respectively.

(6) Comparing the results of different helix angles $\beta 25$, $\beta 20$, $\beta 15$, and $\beta 10°$ and hole ratios $a/b = 1$, a/b = 0.8, $a/b = 0.6$, and $a/b = 0.4$, it was found that the hole plate-type heater with the helix angle $\beta 25°$ and the hole ratio $a/b = 1$ has the highest evaluation index $Nu/f^{1/3}$ and the best overall performance.

(7) The design of the continuous spiral baffle plate perforated-type heater in this well enhances heat transfer between the gas and the perforated heating plate, improves the flow state of the heater shell, avoids local high temperature on the heating plate surface, extends the service life of the heater, and enhances overall performance. This design contributes to the extraction and production of shale oil.

AUTHOR INFORMATION

Corresponding Authors

Hao Liu − *College of Mechanical and Electrical Engineering, Beijing University of Chemical Technology, Beijing 100029, China*; orcid.org/0009-0009-0730-2347; Email: 15103380300@163.com

Yang Zhang − *College of Mechanical and Electrical Engineering, Beijing University of Chemical Technology, Beijing 100029, China*; Email: 2002500011@mail.buct.edu.cn

Authors

Tengfei Sun − *College of Mechanical and Electrical Engineering, Beijing University of Chemical Technology, Beijing 100029, China*

Tingjun Yan − *College of Mechanical and Electrical Engineering, Beijing University of Chemical Technology, Beijing 100029, China*

Complete contact information is available at: https://pubs.acs.org/10.1021/acsomega.3c04099

Author Contributions

†T.S. and H.L. are co-first authors and contributed equally to this work.

Notes

The authors declare no competing financial interest.

ACKNOWLEDGMENTS

The authors gratefully acknowledge the financial support of the National Nature Science Foundation of China (Nos. 52074018, 52274001) and the financial support of fundamental Research Funds for the Central Universities (buctrc202017).

REFERENCES

(1) Tong, X.-G.; Zhang, G.-Y.; Wang, Z.-M.; Wen, Z.-X.; Tian, Z.-T.; Wang, H.-J.; Ma, F.; Wu, Y.-P. Distribution and potential of global oil and gas resources. *Pet. Explor. Dev.* **2018**, *45* (4), 779−789.

(2) Song, R.-R.; Meng, X.-L.; Yu, C.; Bian, J.-J.; Su, J.-Z. Oil shale in-situ upgrading with natural clay-based catalysts: Enhancement of oil yield and quality. *Fuel* **2022**, *314*, No. 123076.

(3) Liu, H.; Sun, T.-F.; Zhang, Y.; Wu, B.-K.; Wang, Z.-L.; Fan, Y.-C. Design of Oil Shale In-Situ Extraction Heater Structure and Numerical Simulation of the Fracturing Process. *Chem. Technol. Fuels Oils* **2023**, *58*, 990−1004, DOI: 10.1007/s10553-023-01481-0.

(4) Wang, L. Experiment and Simulation on thermal conductance during In-situ Oil Shale Mining by electric heating. 2014.

(5) Wang, Z.-D.; Yang, F.; Fu, D.-L.; Duan, Z.-H.; Wang, Q.-W.; Kang, S.-J.; Guo, W. Economic and heating efficiency analysis of double-shell downhole electric heater for tar-rich coal in-situ conversion. *Case Stud. Therm. Eng.* **2022**, *41*, No. 102596, DOI: 10.1016/j.csite.2022.102596.

(6) Wang, Q.-W.; Chen, G.-D.; Xu, J.; Ji, Y.-P. Second-law thermodynamic comparison and maximal velocity ratio design of shell-and-tube heat exchangers with continuous helical baffles. *J. Heat Transfer* **2010**, *132*, No. 101801, DOI: 10.1115/1.4001755.

(7) Peng, B.-T.; Wang, Q.-W.; Chen, Q.-Y.; Zeng, M.; et al. An Experimental Study of Shell-and-Tube Heat Exchangers With Continuous Helical Baffles. *J. Heat Transfer* **2007**, *129* (10), 1425−1431, DOI: 10.1115/1.2754878.

(8) Yang, J.-F.; Zeng, M.; Wang, Q.-W. Numerical investigation on combined single shell-pass shell-and-tube heat exchanger with two-layer continuous helical baffles. *Int. J. Heat Mass Transfer* **2015**, *84*, 103−113, DOI: 10.1016/j.ijheatmasstransfer.2014.12.042.

(9) Sun, Z.-J.; Numerical Simulation and Experimental Study on Downhole Electric Heater with Continuous Helical Baffles. 2017.

(10) Lutcha, J.; Nemcansky, J. Performance improvement of tubular heat exchangers by helical baffles. *Chem. Eng. Res. Des.* **1990**, *68* (A3), 263−270.

(11) Stehlik, P.; Němčanský, J.; Kral, D.; Swanson, L.-W. Comparison of correction factors for shell-and-tube heat exchangers with segmental or helical baffles. *Heat Transfer Eng.* **1994**, *15* (1), 55−65.

(12) Guo, W.; Wang, Z. D.; Sun, Z.-J.; Sun, Y.-H.; Lü, X.-S.; Deng, S.-H.; Qu, L.-L.; Yuan, W.; Li, Q. Experimental investigation on performance of downhole electric heaters with continuous helical baffles used in oil shale in-situ pyrolysis. *Appl. Therm. Eng.* **2019**, *147*, 1024−1035.

(13) Cao, X.; Chen, D.-M.; Du, T.-T.; Liu, Z.; Ji, S. Numerical investigation and experimental validation of thermo-hydraulic and thermodynamic performances of helical baffle heat exchangers with different baffle configurations. *Int. J. Heat Mass Transfer* **2020**, *160*, No. 120181.

(14) Liu, Y.-C.; Wen, J.; Wang, S.-M.; Tu, J.-Y. Numerical investigation on the shell and tube heat exchanger with baffle leakage zones blocked. *Int. J. Therm. Sci.* **2021**, *165*, No. 106959.
(15) Gu, H.-D.; Chen, Y.-P.; Wu, J.-F.; Yang, S.-F. Numerical study on performances of small incline angle helical baffle electric heaters with axial separation. *Appl. Therm. Eng.* **2017**, *126*, 963−975.
(16) Dogan, S.; Darici, S.; Ozgoren, M. Numerical comparison of thermal and hydraulic performances for heat exchangers having circular and elliptic cross-section. *Int. J. Heat Mass Transfer* **2019**, *145*, No. 118731.
(17) Liang, S.; Huang, X.-Q.; Yu, H.-Y. Research of Flowing and Heat Transfer Characteristics for Heat Exchanger with Various Helix Angle in Baffles. *Process Equip. Piping* **2019**, *56* (05), 32−38.
(18) Rezwan, A. A.; Hossain, S.; Rahman, S.-M.-A.; Islam, M.-A. Heat transfer enhancement in an air process heater using semi-circular hollow baffles. *Procedia Eng.* **2013**, *56*, 357−362.
(19) Wang, F.-H. *Computational Fluid Dynamics Analysis-Principles and Applications of CFD Software*; Tsinghua University Press, Beijing, China. 2008.
(20) Tao, W.-Q. *Numerical Heat Transfer*; Xi'an Jiaotong University Press, Xi'an, China. 2005.
(21) Cao, X. Theoretical Analysis and Experimental Study of Shell-and-Tube Heat Exchanger with Continuous Helical Baffles and Overlapped Helical Baffles. 2012.
(22) Ji, S. Meehanism Analysis and Performance Study of Flow and Heat Transfer in Shell-side of Shell-and-Tube Heat Exchanger with Helical Baffles. 2011.
(23) Jafari Nasr, M.-R.; Shafeghat, A. Fluid flow analysis and extension of rapid design algorithm for helical baffle heat exchangers. *Appl. Therm. Eng.* **2008**, *28* (11−12), 1324−1332.
(24) He, Y.-L.; Lei, Y.-G.; Tao, W.-Q.; Zhang, J.-F.; Chu, P.; Li, R. Second-law based thermodynamic analysis of a novel heat exchanger. *Chem. Eng. Technol.* **2009**, *32* (1), 86−92.
(25) Andrews, M.-J.; Master, B.-I. Three-dimensional modeling of a Helixchanger((R)) heat exchanger using CFD. *Heat Transfer Eng.* **2005**, *26* (6), 22−31.
(26) Lei, Y.-G.; He, Y.-L.; Chu, P.; Li, R. Design and optimization of heat exchangers with helical baffles. *Chem. Eng. Sci.* **2008**, *63* (17), 4386−4395.
(27) Yadav, A. S.; Shrivastava, V.; Sharma, A.; Sharma, S. K.; Dwivedi, M. K.; Shukla, O. P. CFD simulation on thermo-hydraulic characteristics of a circular tube having twisted tape inserts. *Mater. Today: Proc.* **2021**, *47*, 2790−2795.
(28) Yadav, A. S.; Shrivastava, V.; Dwivedi, M. K.; Shukla, O. P. 3-dimensional CFD simulation and correlation development for circular tube equipped with twisted tape. *Mater. Today: Proc.* **2021**, *47*, 2662−2668.
(29) Wang, M.- C.; Chen, Y.-P.; Wu, J.-F. Heat Transfer Enhancement of folded Helical Baffle Electric heaters. *J. Eng. Thermophys.* **2016**, *37* (10), 2206−2210.
(30) Gibbons, N.-N.; Damm, K.-A.; Jacobs, P.-A.; Gollan, R.-J. Eilmer: an open-source multi-physics hypersonic flow solver. *Comput. Phys. Commun.* **2023**, *282*, No. 108551.
(31) Sun, B.; Li, C.; Yang, S.-L.; Zhang, H.-J. A simplified method and numerical simulation for wedge-shaped plunger wavemaker. *Ocean Eng.* **2021**, *241*, No. 110023.
(32) Zhang, T.; Li, M.; Guo, J.-C.; Gou, H.-R.; Mu, K.-F. Numerical Study on Mechanism and Parameters Optimization of Temporary Plugging by Particles in Wellbore. *SPE Prod. Oper.* **2022**, *37* (01), 135−150, DOI: 10.2118/208585-PA.
(33) Rakesh, K. Heat exchange simulation of mobile bottle chiller/ Rakesh Kamalakannan. Doctoral dissertation; University of Malaya, 2019.
(34) Yang, S.-M.; Tao, W.-Q. *Heat Transfer Theory*; Higher Education Press, Beijing, China, 2006.
(35) Gu, X.; Wang, T.-T.; Chen, W.-J.; Luo, Y.-K.; Tao, Z.-L. Multi-objective optimization on structural parameters of torsional flow heat exchanger. *Appl. Therm. Eng.* **2019**, *161*, No. 113831.
(36) Xu, W.-F. Numerical Study on Heat Transfer Enhancement of Helical Baffles Heat Exchanger and Optimization of baffles Structure. 2016.
(37) Gan, L.-Y. Analysis of flow and heat transfer characteristics and structure optimization of spiral plate heat exchanger. 2021.

https://doi.org/10.1021/acsomega.3c04099
ACS Omega 2023, 8, 36043−36052